

## METHODOLOGY ASSESSMENT FOR THE DESIGN AND ANALYSIS OF AERO-ENGINE SHORT INTAKES

Luca Boscagli <sup>(1)</sup>, Robert Christie <sup>(2)</sup>, David G. MacManus <sup>(2)</sup>

<sup>(1)</sup> Cranfield University, MK43 0AL, Cranfield, UK, Email: luca.boscagli@cranfield.ac.uk

<sup>(2)</sup> Cranfield University, MK43 0AL, Cranfield, UK

**KEYWORDS:** short intake, fan coupling, flow distortions, unsteady

### ABSTRACT

A key aspect for the design of an aero-engine intake is that it must operate at off-design conditions such as high incidence. For short intake design the interaction with the fan cannot be neglected. This work establishes how different modelling strategies can affect the intake design boundaries and the analysis of an aero-engine short-intake. Unsteady simulations showed high levels of total pressure and swirl fluctuations while steady computations showed some limitations whenever extreme operating conditions are modelled. The analysis of a short intake showed that the fan is able to extend the incidence limit to avoid separation by about  $0.6^\circ$ . Overall, this work proposes a robust methodology for short-intake analysis.

### 1. INTRODUCTION

The next generation of high efficiency turbofans will be characterised by larger fan diameters, which in turn could lead to an increase in nacelle weight and drag. These two negative effects can be partially counteracted through the installation of a shorter inlet and exhaust duct. However, the design of a short intake can be challenging because of the reduced internal diffusion capability and the non-negligible interaction of the flow between the intake and the fan. This can be of highest importance during take-off, climb-out and crosswind conditions where a distorted flow may be expected. Moreover, at these conditions the flow along the lip can locally reach a supersonic regime. Thus, shockwaves rise into the flow field and separation and unsteadiness might occur (Fig. 1). Coschignano [1,2] conducted a 2D experimental study of such a Shock-Wave Boundary Layer Interaction (SWBLI). Through Schlieren visualisations and pressure sensitive paint, the occurrence of a 'lambda shock-wave' and separation onset were investigated as a function of the angle of attack. A parametric study also revealed the impact of lip shape on SWBLI.

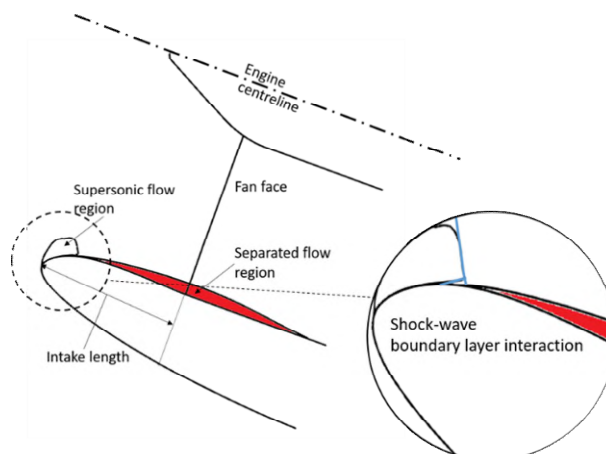


Figure 1. Flow features within an aero-engine intake at high incidence (after [1])

Peters [3] provided an insight into a range of potential issues for short intake design. The key finding was that the design of a short intake seems to be limited by a region of high Mach number at the fan face which leads the rotor to operate close to choke. This resulted in an increase of distortion levels and a reduction of fan operability. Several recent publications addressed the problem of fan-intake interaction from different perspectives. Cao [4] provided an extensive numerical study on fan interaction with separated flow within an intake at high incidence. Depending on the ratio between the length of the intake ( $L_{in}$ ) and the fan diameter ( $D_{fan}$ ), the fan can either reduce the distortion levels after separation or delay the separation onset. Ma [5] assessed the influence of turbulence modelling with respect to fan modelling. Large Eddy Simulations (LES) and Reynolds-Averaged Navier-Stokes (RANS) simulations combined with a lower order model for the fan [6,7] were compared. The main conclusion was that the mass flow redistribution due to the fan has a primarily effect on intake flow turbulence. Thus, higher fidelity methods, such as eddy resolving simulations, might only produce marginal improvements on the level of accuracy of the results. Carnevale [8] considered a full assembly intake, fan, bypass and pylon and addressed the coupled problem through a fan similarity model [9]. This simplified model showed that the fan-intake interaction involves mainly the lower frequencies.

Several studies have tackled the same problem from the fan point of view. Zhang [10] carried out a parametric study about the effect of inlet distortions on the prediction of fan stall. Within the context of a complex intake and Boundary Layer Ingestion (BLI), Provenza [11] showed how the frequency content of inlet flow distortions can affect the fan at 1 Engine Order (EO), thus limiting the fan operability range. Also, overall fan performances were affected by highly disturbed flow developing along the intake. Gunn [12] highlighted how inlet distortions can lead to a 5.3% reduction in stage total-to-total efficiency. Within this context, the current work establishes a methodology to analyse short intake performance at high incidence in order to provide design boundaries and a better understanding of the fan-intake interaction mechanism.

## 2. METHODOLOGY

### 2.1. Solver

A high-resolution scheme was used for spatial discretisation [13]. The scheme is nominally second order where the solution is smooth, but it recovers first order accuracy whenever the solution is discontinuous. This is due to the Godunov theorem and the inability to construct a monotonicity preserving scheme with an accuracy higher than first order. For the unsteady calculations, an implicit second order scheme was used for the time discretization.

### 2.2. Computational grid

A structured meshing strategy was developed to target a  $y^+ = 1$  within the domain of interest. As a check, a boundary layer profile computed at the fan face and scaled in wall units was plotted on a semilog-scale against the 'law of the wall'. The good agreement with the theoretical values has confirmed the good mesh quality in terms of  $y^+$  resolution (Fig. 2).

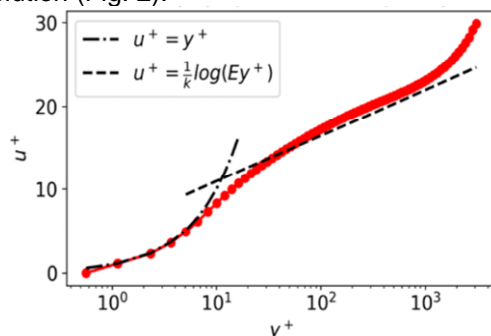


Figure 2. Law of the wall. Boundary layer profile extracted at the fan face at the top aeroline. Results obtained from kw-SST model.

For the aspirated intake configuration this resolution was matched within the whole intake domain. However, for the powered case with the intake and fan stage a  $y^+ = 1$  within the fan domain is unfeasible since it would result in a large increase in mesh size. This would make both steady and unsteady computations expensive. The use of a wall function and a coarser mesh in terms of  $y^+$  resolution can reduce the computational cost. Thus, a single blade passage fan model was studied using two different meshes. A wall function approach for the fan was proven to be adequate with a prediction of fan adiabatic efficiency within 1% of measurements.

Greater effort was spent on trying to make the intake mesh and the fan mesh as conformal as possible. To achieve that, the first cell height at the fan shroud was set in order to match that on the intake side. The same approach was adopted for the spinner, where part of the geometry is in the intake domain and part is in the fan domain. This avoids discontinuities in the development of the boundary layer moving from one domain to the other. Following these meshing strategies, the mesh size of the full assembly was about  $40 \times 10^6$  elements. For the aspirated configurations the mesh comprised  $14 \times 10^6$  hexahedral elements.

### 2.3. Boundary conditions

For the powered configuration a fully coupled problem was considered. Intake, full-annulus fan, one passage Outlet Guide Vane (OGV) and one passage Engine Section Stator (ESS) were modelled. At the interface between the fan and the intake a frozen rotor approach was considered for the steady simulations, while a transient rotor-stator interface boundary condition was applied for the transient simulation [13]. At the two interfaces of the fan with the OGV and the ESS, uniform circumferentially averaged boundary conditions were applied since only one passage each was modelled.

## 3. RESULTS AND DISCUSSION

### 3.1. Aspirated configuration

Baseline validation analyses were done for a non-axisymmetric intake geometry characterised by  $L_{IN}/D_{fan} \approx 0.6$ . Typical values of  $L_{IN}/D_{fan}$  for short intake range from 0.25 to 0.5. Thus, the present geometry cannot be considered a short intake. The wind tunnel model was instrumented with standard Pitot probes at the Aerodynamic Interface Plane (AIP) as well as static pressure tapings along the intake lip and diffuser. Total pressure distortion was quantified based on DC60 (Eqn. 1) [14,15],

$$DC60 = \frac{\overline{P_{0,60}} - \overline{P_{0,AIP}}}{\overline{q_{AIP}}} \quad (1)$$

In Eq. 1  $\overline{P_{0,60}}$  is the lowest area-averaged total pressure in a 60° sector at the AIP,  $\overline{P_{0,AIP}}$  and  $\overline{q_{AIP}}$

viscosity models, Spalart-Allamaras (SA) and kw-SST, were tested and compared against the experimental results in terms of isentropic Mach profiles along the lower section of the intake lip. For both models a curvature correction was used [17].

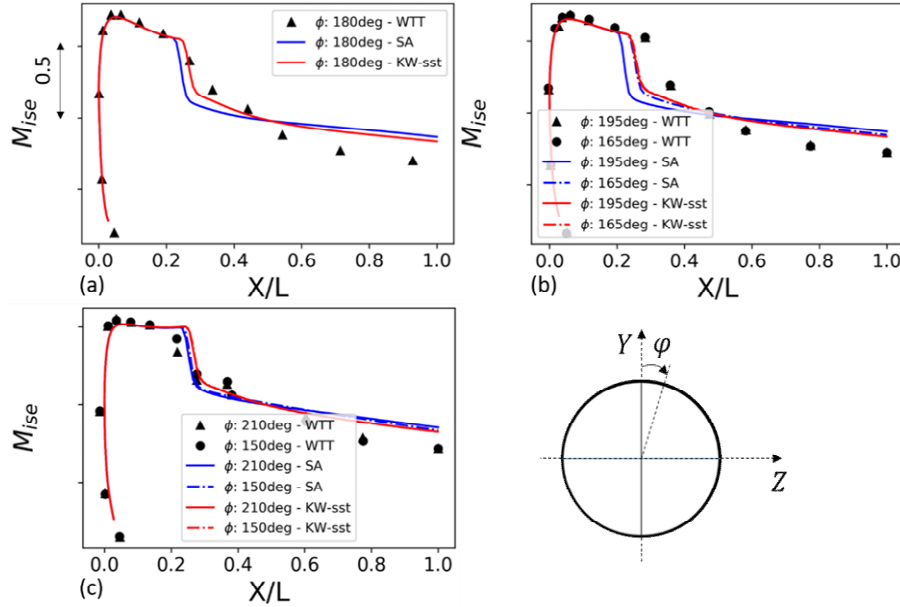


Figure 3. Isentropic Mach profiles at 'pre-separation' point. Comparison between SA and kw-SST turbulence models against wind tunnel data

are the area-averaged total pressure and dynamic head, respectively. For the computation of the distortion metrics the CFD results were extracted at the same positions as the Pitot probes and area averaged in the same way as the measurements. Moreover, for the unsteady simulations, the CFD data were filtered according to the frequency response of the pressure probes used in the experiments.

### 3.1.1. Turbulence model assessment

Shock-wave boundary layer interaction is a well known problem which can lead to the formation of a 'lambda shock-wave' [16]. It is affected by pre and post shock Mach number as well as by the shape factor of the boundary layer. This is in turn a function of Reynolds number and pressure gradient [2]. Thus, both computational and experimental modelling is a challenging task.

From a purely computational point of view, whenever RANS equations are solved to model the flow field, the boundary layer development is predicted through a turbulence model. A convective-diffusion equation is solved where the modelling of the 'production' term can be based on different hypothesis. This will in turn affect the prediction of separation onset. Two different eddy-

For the SA model the production term is based on the entire deviatoric part of the velocity gradient tensor. Thus, it predicts eddy viscosity production based both on strain rate and vorticity levels. Including the strain tensor in the production term was shown to limit the over-prediction of eddy viscosity in the areas where the vorticity exceeds the strain rate [18].

The performance of the two turbulence models was investigated and a comparison with the experimental data was assessed in terms of isentropic Mach ( $M_{ise}$ ) distributions along the intake lip and diffuser (Fig. 3). The operating conditions were classified as 'pre-separation point' in the wind tunnel experiments. The distributions were measured at five different azimuthal locations ( $\phi$ ). Both turbulence models are able to capture the peak  $M_{ise}$  when compared with the experimental results (Fig. 3). At  $\phi = 180^\circ$  kw-SST is in better agreement with the measurements relative to the SA calculations in terms of capturing the shock position (Fig. 3a). On the other hand, the performance of both turbulence models degrades in the post-shock region where there is a notable discrepancy from the experimental values. At two off-centre positions with respect to the meridional plane there is a lack of symmetry in the SA results

(Fig. 3b). That might be an indication of increasing unsteadiness in the flow field.

Thus, the present results suggest an overall better performance of the  $k\omega$ -SST model which was selected for the subsequent analysis.

### 3.1.2. Steady and unsteady analysis

At high incidence, post separation the flow inside an intake is characterised by high levels of distortions and unsteadiness. Thus, an assessment of the accuracy of steady RANS in the identification of the design boundaries is useful through a comparison with experimental results and unsteady simulations. The Angle of Attack (AoA) was gradually increased by  $0.2^\circ$  and its effect on DC60 was evaluated. Mass Flow Capture Ratio (MFCR) was 1.5 and freestream Mach number was 0.29. The distribution of DC60 shows a sudden increase for a critical angle of attack ( $\alpha_c$ ) at which condition the DC60 exceeds a threshold value (Fig. 4). This indicates that significant separation within the intake reaches the measurement section and the onset of unsteadiness occurs. Unsteady analysis was performed to capture this behaviour and to provide a better understanding of the characteristics of the flow.

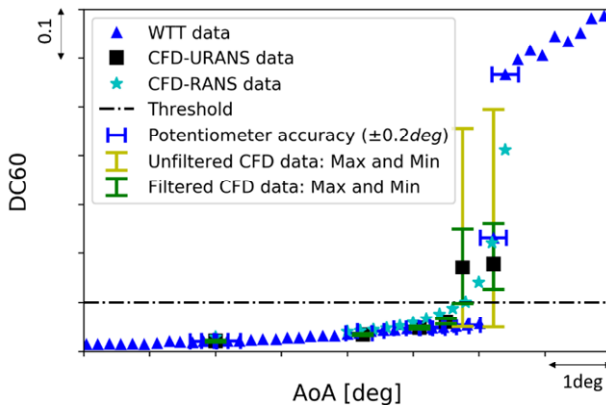


Figure 4. Effect of angle of attack sweep on DC60

Both the steady and unsteady simulations show a good agreement with the experimental results (Fig. 4). The critical AoA ( $\alpha_c$ ) was calculated within about  $0.5^\circ$ . This discrepancy is of the same order of magnitude of the accuracy of the potentiometer ( $\pm 0.2^\circ$ ) used in the experiments. Range bars were attached to the unsteady results (Fig. 4). These represent the maximum and minimum peak values from the simulations. Also, both the filtered and unfiltered values were reported.

To provide a better insight to the characteristics of the flow field at high incidence, DC60 distribution was analysed through unsteady simulations. A characteristic timescale (convective time,  $t_c$ ) was

computed based on the length of the intake and the mean flow velocity within it. Once a statistically converged solution was obtained based on the standard error of DC60 time history, about 45 through-flow times ( $t/t_c$ ) were retained and post-processed.

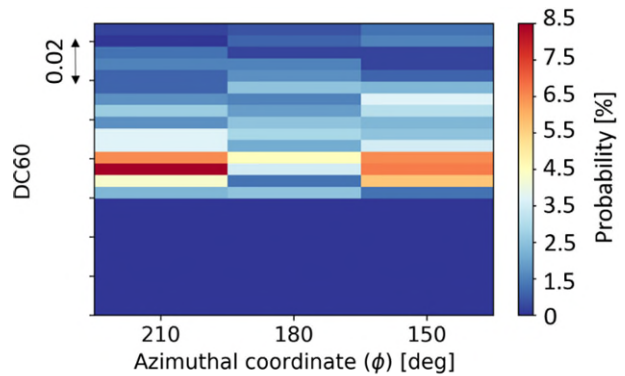


Figure 5. Filtered azimuthal distribution of unsteady DC60, coloured with the probability of occurrence

The azimuthal distribution of DC60 at the AIP was investigated (Fig. 5). In accordance with the experiments, it was computed with a  $30^\circ$  azimuthal resolution. The colour range represents the probability of occurrence of a certain value of DC60 at a certain azimuthal position. The plot highlights a clear lack of symmetry in the DC60 distribution and it also shows that the main loss region is off centre. This confirms the necessity in the experimental set up to have a good azimuthal resolution on both side of the lower aeroline of the intake. Also, the present analysis points out the inherently 3D nature of the flow field within an intake at high incidence.

The unsteady simulations provided useful information about the high levels of total pressure and swirl distortions that occur at the fan face (Fig. 6). Swirl angle peaks above  $20^\circ$  were also noted throughout the computation. This might have an impact in experimental investigations where the response of standard Pitot probes highly deteriorates for flow deviation above  $11-12^\circ$ .



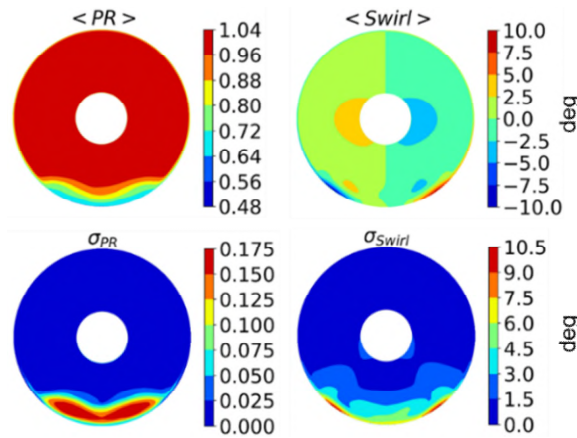


Figure 6. On the first row, time averaged mean values of total pressure ratio fluctuations (left) and swirl angle fluctuations (right). On the second row, standard deviation of the same quantities

For the greatest angle of attack, a spectral analysis of total pressure and swirl fluctuations at the AIP was done. Strouhal number ( $St$ ) is based on the average axial velocity at the fan face ( $\overline{U_{x,fan}}$ ) and the fan diameter ( $D_{fan}$ ). A clear spectral signature was identified for both total pressure and swirl fluctuations within the Strouhal band ranging from  $St = 0.28$  and  $St = 0.42$  (Fig. 7). This may be relevant for fan transient dynamics and unsteady characteristics. For a model scale, fan modes at 1EO are typically characterised by values of Strouhal number of  $\sim 0.7$  [11].

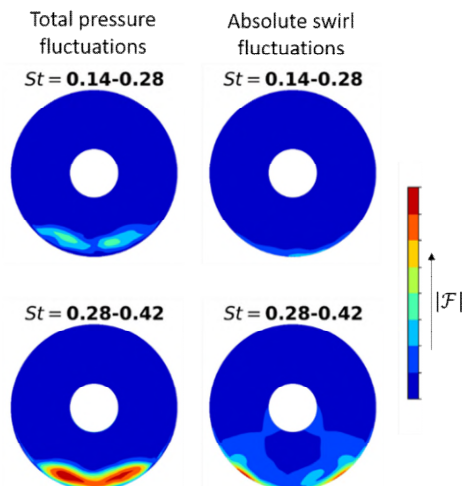


Figure 7. Strouhal bands obtained through spectral analysis of total pressure fluctuations (left) and swirl angle fluctuations (right)

### 3.2. Powered configuration

A powered configuration of a short intake ( $L_{in}/D_{fan} = 0.35$ ) was investigated based on the modelling experience from the previous analysis. For the turbomachinery components, the whole fan annulus was modelled while only one blade passage was included for both the OGV and ESS. Due to the simplification on the stator group, different boundary conditions were applied at the interfaces in the whole intake-fan domain. A frozen rotor approach [13] was used at the fan-intake interface, while uniform circumferentially averaged boundary conditions were applied at the two interfaces between fan-OGV and fan-ESS. Thus, OGV and ESS feedback mechanism due to total pressure distortions at the fan face was assumed to be negligible from the intake point of view. A fan tip gap of  $\sim 0.1\%$  fan radius was modelled. This might be expected to influence both fan performances and the flow within the intake. Also, an aspirated configuration was studied in order to quantify the influence of the fan on the intake distortions. The aspirated geometry only differs from the powered configuration where the shape of the casing in the fan domain was modified. The aspirated configuration includes a cylindrical shroud downstream of the fan face. The extended duct limits the influence of the boundary conditions imposed at the fan outlet on the flow along the intake.

The fan may be expected to reduce intake flow distortions by changing curvature of the flow streamlines and closing the recirculation bubble by enhancing the turbulence transport [6]. A low-order fan model was previously used to simplify the fan geometry by modelling an infinite number of blades (smeared geometry, [7]). On the other hand, frozen

rotor approach is affected by the fan blades position within the computational grid. The fan-intake interaction and the upstream propagation of acoustic waves may be expected to be a function of the position of the fan blades. Thus, a 'fan-clocking' study with a frozen rotor model was performed. This is also required for a fair comparison with unsteady simulations. The fan pitch angle is  $20^\circ$  so the fan blades were progressively rotated by  $4^\circ$  and 5 configurations were generated. For consistency, both  $0^\circ$  and  $20^\circ$  blade relative position were investigated. A total of 6 frozen rotor configurations were modelled.

The intake flow distortion was evaluated at an Aerodynamic Interface Plane (AIP) which was positioned at 10% of the fan radius upstream of the fan face. This provided the largest levels of total

pressure distortions and thus it was used to be more conservative to identify intake design boundaries.

The effect of Angle of Attack (AoA) on DC60 was investigated (Fig. 8a). An aspirated configuration of the same intake geometry was also studied to quantify the effect of the fan. In this case the AoA was gradually increased by  $0.2^\circ$  around the expected critical AoA ( $\alpha_c$ ). At relatively low AoA the DC60 distribution obtained from the different fan-clocking studies showed that there is not a significant influence of the fan blade azimuthal position on the flow field within the intake.

As the AoA increases one of the configurations (Fig. 8a – 'Blade pos.: 4deg') shows a steeper increase in DC60 value which exceeds the threshold. This establishes the critical AoA ( $\alpha_c$ ) for the short intakes

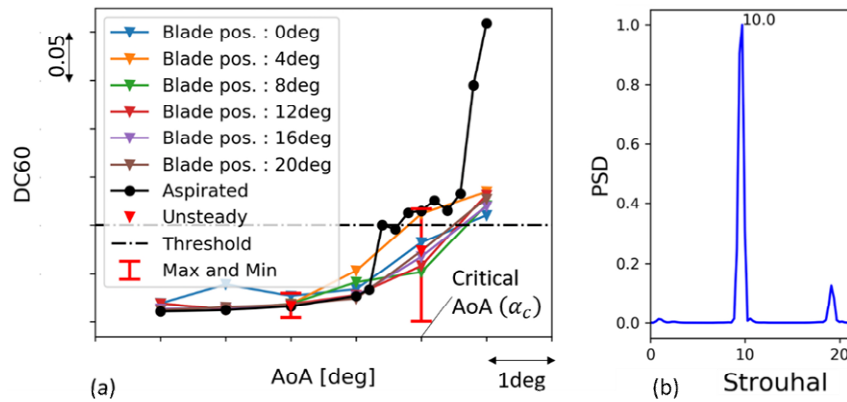


Figure 8. AIP located at 10% fan radius upstream of the fan face. On the left, effect of angle of attack sweep on DC60. On the right normalized Power Spectral Density of DC60 time history as a function of Strouhal number obtained from transient simulation at  $\text{AoA} = \alpha_c - 2^\circ$

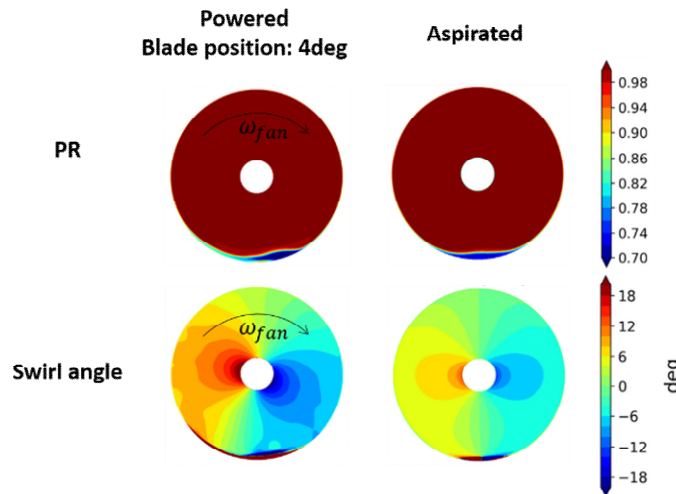


Figure 9.  $\text{AoA} = \alpha_c$ . RANS computations. AIP located at 10% fan radius upstream of the fan face. On the first row total pressure ratio contours at AIP. On the second row absolute swirl angle

and identifies the intake design boundaries. Compared with the aspirated configuration this also

region of high total pressure distortion. The appearance of a shock-wave along the lip led to

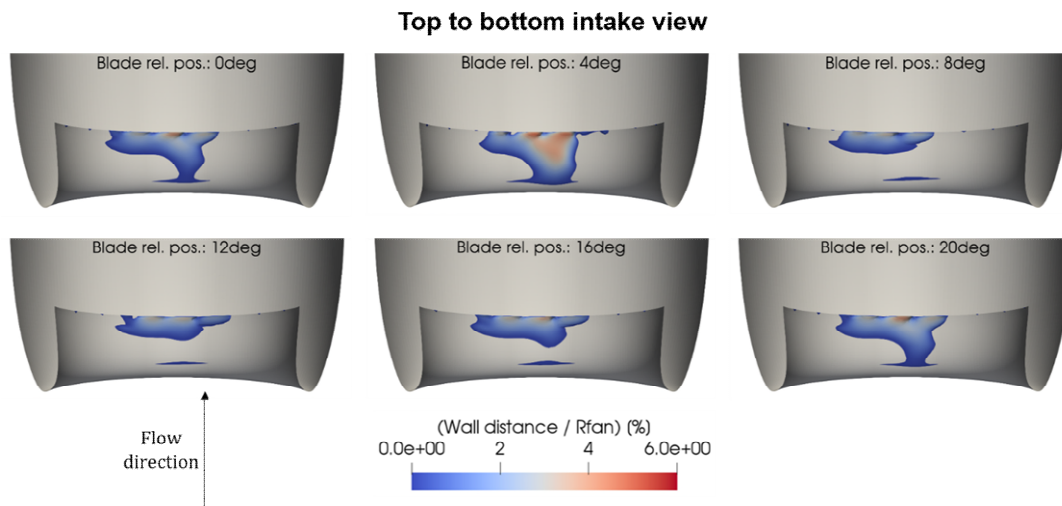


Figure 10. Top to bottom intake view.  $\text{AoA} = \alpha_c$ . Frozen rotor computations. Iso-surfaces of zero axial velocity coloured with wall distance as a percentage of the fan radius

highlights that the fan has recovered intake total pressure distortion and it has reduced the critical AoA by  $\sim 0.6^\circ$ . At  $\alpha_c$  the flow field at the AIP looks

leading edge separation.

The frozen rotor study indicated an influence of the position of the fan blades at higher AoA. Thus, an

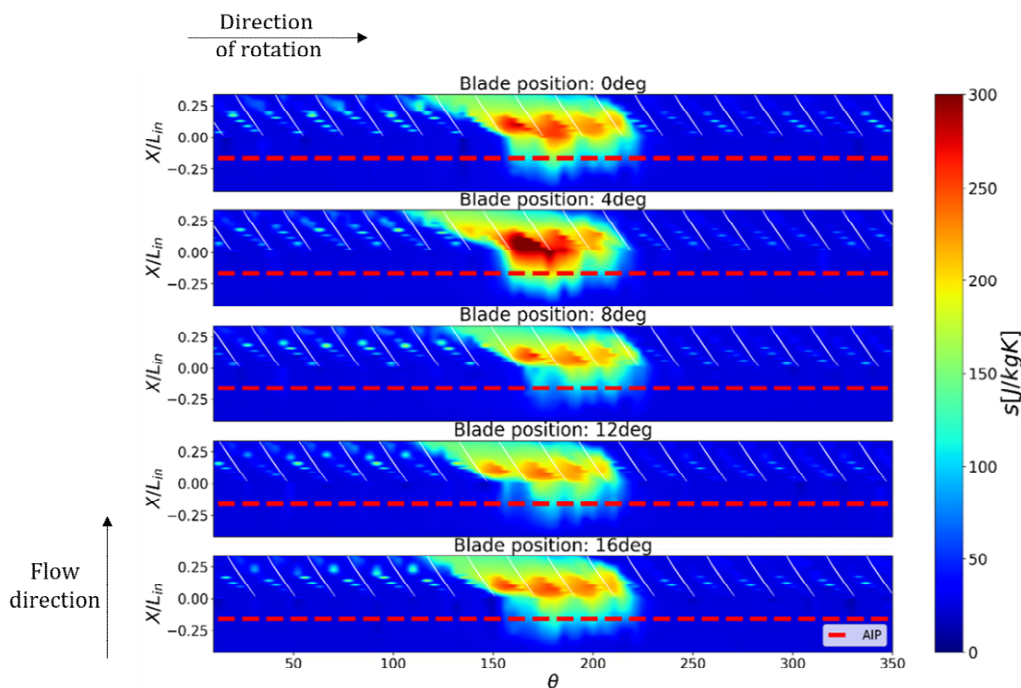


Figure 11.  $\text{AoA} = \alpha_c$ . Frozen rotor computations. Azimuthal distribution of static entropy within intake and fan domain at 95% of fan radius

similar for the aspirated and powered configuration, although the presence of the fan makes the flow inherently asymmetric (Fig. 9). For the powered configuration the blade loading increased in the

in-depth analysis of the flow field at the critical AoA was performed. The separated region within the intake showed some differences depending on the blade position (Fig. 10). All the configurations



present a shock-induced separation along the lip and diffusion induced separation within the diffuser. For two blade positions ( $0^\circ \equiv 20^\circ$  and  $4^\circ$ ) these two separated regions merge. This is consistent with the higher values of DC60 (Fig. 8a). The azimuthal distribution of static entropy at 95% of the fan radius shows high levels of losses within the fan in agreement with the high DC60 value and large separation region (Fig. 11). Inlet flow distortions also caused high levels of counter-rotating swirl which increases the blade loading (Fig. 12). Blade incidence angle is also affected by the position of the blade as a result of the different swirl angle.

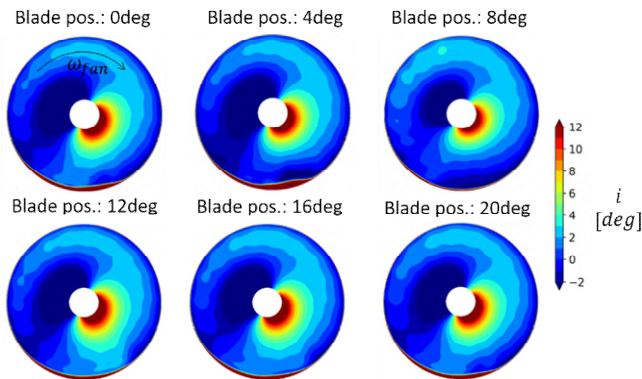


Figure 12.  $AoA = \alpha_c$ . AIP located at 10% fan radius upstream of the fan face. Frozen rotor computations. Contour plot of blade relative incidence angle for each fan-clocking position

However, the studies presented in the previous section showed that the onset of unsteadiness within the flow field might also be expected. Thus, a transient simulation was performed to provide a comparison with the frozen rotor results and to understand the likely impact on the intake design requirements. This might be expected to give also a better insight in the fan-intake interaction mechanism.

The coupling between fan and intake requires some a priori considerations in order to construct a transient simulation and to provide a reliable description of the interaction mechanism. The selection of the sampling frequency requires the estimation of a relevant timescale length. The fan rotation determines a key timescale length for the present problem setup and operating conditions. Thus, based on fan rotational speed and pitch angle, a blade passing time was computed. For an accurate representation of the spectrum, each blade passing was solved with 20 timesteps by selection of a sample frequency corresponding to a Strouhal number of 10. This provided a  $1^\circ$  azimuthal resolution in the fan mesh movement. On the other hand, the selection of the observation time required

some theoretical considerations. The fan-intake interaction mechanism was assumed to be related to potential flow characteristics. From the eigenstructure of the Euler equations, one can have an estimate of the propagation velocity of different waves. Thus, the longest timescale related to this process was computed through an assessment of the axial location of the shock-wave.

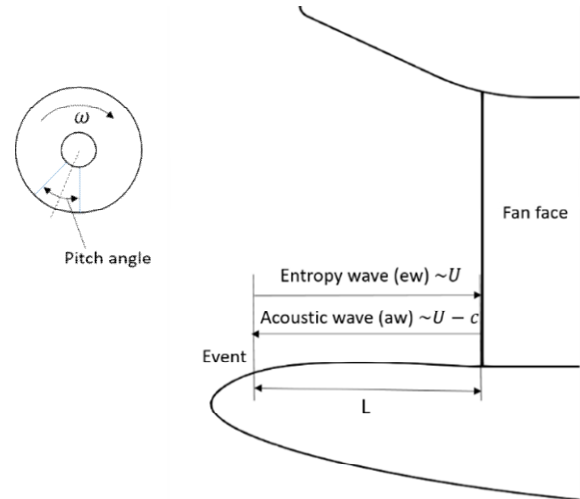


Figure 13. Sketch of transient mechanism of interaction between the intake and the fan

The time for a complete fan-intake interaction cycle was estimated based on the propagation time of the upstream travelling acoustic wave and the propagation time of the downstream travelling entropy wave (Fig. 13). The first one travels with the speed of sound relative to the mean flow velocity, while the second one moves with the mean flow velocity. For the present case this characteristic time was found to be about 6 blade-passing time ( $t_b$ ). Thus, a preliminary unsteady analysis was performed at an  $AoA$   $2^\circ$  lower than the critical  $AoA$  ( $\alpha_c$ ). The AIP located at 10% fan radius upstream of the fan face was sampled every second time step. The value of DC60 at  $AoA = \alpha_c - 2^\circ$  is in agreement with the one obtained through the frozen rotor approach (Fig. 8a). The peak values are within a relatively narrow range thus confirming the limited influence of the blade position on intake distortions. The power spectral density of the DC60 time history shows a peak at a Strouhal number corresponding to that one based on the blade-passing frequency (Fig. 8b). Thus, no frequency content related to flow unsteadiness was found. Also, the distribution of blade incidence angle at AIP only shows peaks up to  $1^\circ$  in the rms values (Fig. 14).



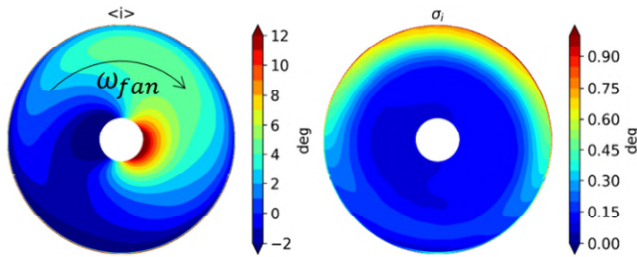


Figure 14.  $AoA = \alpha_c - 2^\circ$  Transient computations. AIP located at 10% of fan radius upstream of the fan face. On the left time-average values of blade incidence angle; on the right standard deviation of the same quantity

These were all expected results due to the relatively low  $AoA$ . However, they confirmed the validity of the initial assumptions made to estimate the most relevant timescales within the flow field. Thus, a transient simulation was then performed at the critical  $AoA$ .

The transient data for two blade revolutions were discarded and four more were computed to reach a statistically converged simulation. The mean time-average DC60 value falls within the range of values computed from the fan-clocking studies (Fig. 8a). However, the peak value exceeds the threshold and agrees with the one computed through a frozen rotor approach for a blade azimuthal position classified as  $4^\circ$ . This confirms the influence of the fan blade position on the intake total pressure distortion that was also observed through the steady computations. The result also confirmed that for the present short-intake geometry the fan improves intake flow distortion by about  $0.6^\circ$  with respect the aspirated case. The RANS results were averaged over all the investigated fan-clocking configurations and comparison of the flow field at the AIP with time averaged unsteady results showed some discrepancy (Fig. 15). Frozen rotor computations predicted larger blade incidence angle within the region of higher total pressure distortions in the intake. Also, the loss region is off centre for the RANS computations and it is located at the azimuthal position where higher values of counter-rotating swirl were found (Fig. 9). Two AIP snapshots from the unsteady model associated with the DC60 maximum and minimum values showed changes within the flow field in terms of both total pressure and swirl angle (Fig. 16). As expected this is associated to the presence of unsteadiness in the flow field. This is confirmed by the isentropic Mach profiles on the lower intake lip (Fig. 17). The difference in peak isentropic Mach between the two timesteps associated with DC60 peak values was found to be about 0.01.

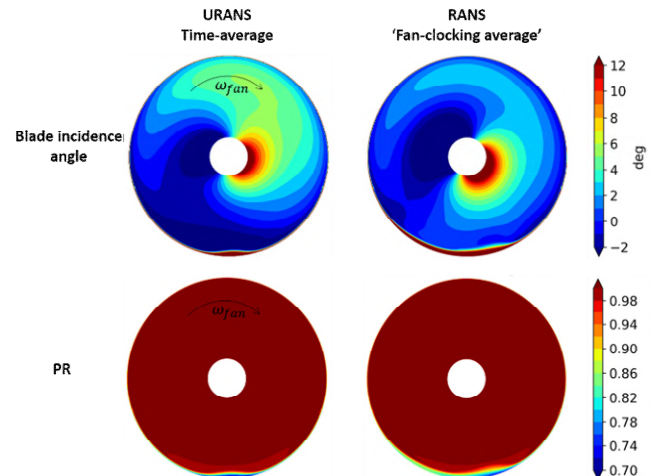


Figure 15.  $AoA = \alpha_c$ . AIP located at 10% of fan radius upstream of the fan face. On the first column URANS time average values. On the second column spatial average of frozen rotor results

The shock location changes between the two timesteps and it is closer to the intake lip leading edge for the case characterised by higher total pressure distortion. The occurrence of the shock wave closer to the lip caused an earlier separation in a region of higher geometric curvature followed by a region of adverse pressure gradient. This caused a larger separation within the intake and higher levels of total pressure distortions at the AIP as highlighted by the DC60 value (Fig. 8a). Also, a phase shift between total pressure distortion at the AIP and the intensity of the shock-wave along the lip might be expected (Fig. 13).

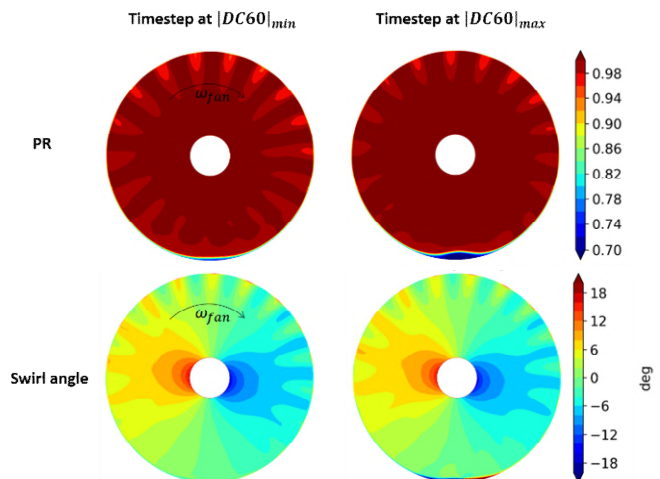


Figure 16.  $AoA = \alpha_c$ . Transient computation. AIP located at 10% of fan radius upstream of the fan face. AIP snapshots corresponding to maximum and minimum value of DC60

Fourier analysis of DC60 time history showed two main peaks (Fig. 18). The one at  $St \approx 10$  is consistent with the one observed at lower AoA (Fig. 8b) and it is related to the blade passing frequency. However, a second peak at  $St \approx 0.28$  is also present at critical AoA. This is related to the onset of unsteadiness in the flow field within the intake.

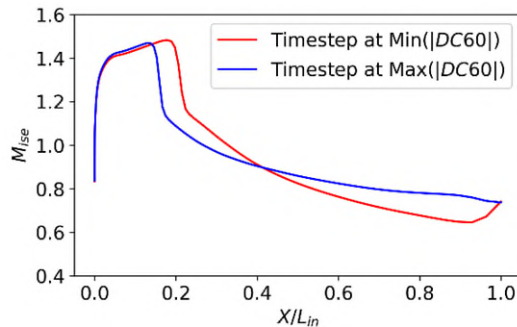


Figure 17.  $AoA = \alpha_c$ . Transient computation. Isentropic Mach profiles on the lower intake lip. Timesteps selected as in Fig. 16

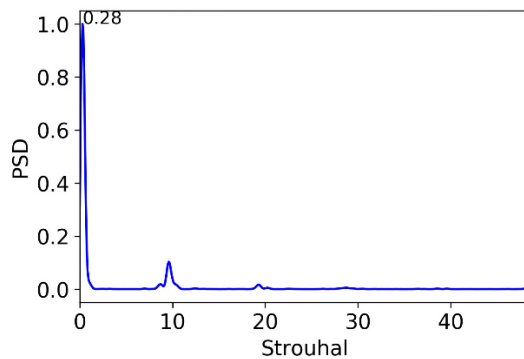


Figure 18.  $AoA = \alpha_c$ . Transient computation. Normalized Power Spectral Density of DC60 time history as a function of Strouhal number

#### 4. CONCLUSIONS

The present work aimed at establishing a methodology to analyse aero-engine short intakes at high incidence. An aspirated intake with  $L_{IN}/D_{fan} \approx 0.6$  was first investigated and results compared against experimental data. This provided a better understanding of the flow features and more confidence on preliminary modelling choices such as turbulence modelling and mesh resolution. The  $k\omega$ -SST model provided a better agreement with the experimental data with respect to SA. An unsteady analysis of the same geometry at higher AoA provided an insight of the unsteady flow distortions, both in terms of peak values and frequency content. High levels of swirl and total pressure fluctuations

characterise the flow field. The Fourier analysis showed a clear spectral signature at  $St \approx 0.4$ . This might be of consideration for the fan dynamic response of the 1EO component.

A non-axisymmetric short intake ( $L_{IN}/D_{fan}$ ) was analysed. Both an aspirated and a powered configuration were investigated to quantify the effect of the fan on distortion reduction and to identify the operational boundaries. Both steady and unsteady simulations predicted the same critical AoA and confirmed that for the investigated short-intake geometry the fan improves total pressure distortions by about  $0.6^\circ$  with respect the aspirated case.

#### 5. ACKNOWLEDGEMENTS

This work is partially funded by Rolls-Royce plc..

#### 6. REFERENCES

1. Coschignano, A., & Babinsky, H. (2018). Normal Shock Wave-Turbulent Boundary Layer interactions in transonic intakes at incidence. In *2018 AIAA Aerospace Sciences Meeting* (p. 1513).
2. Coschignano, A., Atkins, N., Babinsky, H., & Serna, J. (2019). Effect of Reynolds number on a normal shock wave-transitional boundary-layer interaction over a curved surface. *Experiments in Fluids*, 60(12), 185.
3. Peters, A., Spakovszky, Z. S., Lord, W. K., & Rose, B. (2015). Ultrashort nacelles for low fan pressure ratio propulsors. *Journal of Turbomachinery*, 137(2), 021001.
4. Cao, T., Vadlamani, N. R., Tucker, P. G., Smith, A. R., Slaby, M., & Sheaf, C. T. (2017). Fan-intake interaction under high incidence. *Journal of Engineering for Gas Turbines and Power*, 139(4), 041204.
5. Ma, Y., Vadlamani, N. R., Cui, J., & Tucker, P. G. (2018). Comparative Studies of RANS versus LES for Fan-intake Interaction. ASME.
6. Ma, Y., Cui, J., Vadlamani, N. R., & Tucker, P. (2018). Effect of fan on inlet distortion: Mixed-fidelity approach. *AIAA Journal*, 56(6), 2350-2360.
7. Cao, T., Hield, P., & Tucker, P. G. (2017). Hierarchical immersed boundary method with smeared geometry. *Journal of Propulsion and Power*, 33(5), 1151-1163.

8. Carnevale, M., Wang, F., & Di Mare, L. (2018). Calculation of Intake-Fan-Bypass Interaction With a Fan Similarity Model. In *ASME Turbo Expo 2018: Turbomachinery Technical Conference and Exposition*. American Society of Mechanical Engineers Digital Collection.
9. Carnevale, M., Wang, F., Parry, A. B., Green, J. S., & Di Mare, L. (2018). Fan similarity model for the fan–intake interaction problem. *Journal of Engineering for Gas Turbines and Power*, 140(5), 051202.
10. Zhang, W., & Vahdati, M. (2019). A Parametric Study of the Effects of Inlet Distortion on Fan Aerodynamic Stability. *Journal of Turbomachinery*, 141(1).
11. Provenza, A. J., Duffy, K. P., & Bakhle, M. A. (2019). Aeromechanical Response of a Distortion-Tolerant Boundary Layer Ingesting Fan. *Journal of Engineering for Gas Turbines and Power*, 141(1), 011011.
12. Gunn, E. J., Tooze, S. E., Hall, C. A., & Colin, Y. (2013). An experimental study of loss sources in a fan operating with continuous inlet stagnation pressure distortion. *Journal of Turbomachinery*, 135(5), 051002.
13. CFX, A. 18.2 (2018). *ANSYS CFX Manager User's Guide*, Ansys Inc.
14. Seddon, J., & Goldsmith, E. L. Intake Aerodynamics (1985). *AIAA education series*.
15. MacManus, D. G., Chiereghin, N., Prieto, D. G., & Zachos, P. (2017). Complex aeroengine intake ducts and dynamic distortion. *AIAA Journal*, 2395-2409.
16. Stewartson, K. (1951). On the interaction between shock waves and boundary layers. In *Mathematical Proceedings of the Cambridge Philosophical Society* (Vol. 47, No. 3, pp. 545-553). Cambridge University Press.
17. Fluent, A. N. (2017). 18.2, Theory Guide, ANSYS Inc. *Canonsburg, PA*.
18. Dacles-Mariani, J., Zilliac, G. G., Chow, J. S., & Bradshaw, P. (1995). Numerical/experimental study of a wingtip vortex in the near field. *AIAA journal*, 33(9), 1561-1568.



2020-02-28

# Methodology assessment for the design and analysis of aero-engine short intakes

Boscagli, Luca

CEAS

---

Boscagli L, Christie R, MacManus DG. (2020) Methodology assessment for the design and analysis of aero-engine short intakes. In: Aerospace Europe Conference 2020 (AEC2020) 25-28 February 2020, Bordeaux, France

<https://www.cleansky.eu/event/aerospace-europe-conference-eac2020>

*Downloaded from Cranfield Library Services E-Repository*